Remote Sensing of Environment 221 (2019) 210–224

Contents lists available at ScienceDirect

Remote Sensing of Environment

journal homepage: www.elsevier.com/locate/rse

Clarifying the role of radiative mechanisms in the spatio-temporal changes of land surface temperature across the Horn of Africa

Temesgen Alemayehu Abera[a,b,*], Janne Heiskanen[a,b], Petri Pellikka[a,b], Miina Rautiainen[c,d], Eduardo Eiji Maeda[a]

[a] Department of Geosciences and Geography, University of Helsinki, P.O. Box 68, FI-00014, Finland
[b] Institute for Atmospheric and Earth System Research, Faculty of Science, University of Helsinki, Finland
[c] Department of Built Environment, School of Engineering, Aalto University, Finland
[d] Department of Electronics and Nanoengineering, School of Electrical Engineering, Aalto University, Finland

ARTICLE INFO

Keywords:
Albedo
Growing period
Land cover change
Radiative forcing
Land surface temperature
MODIS

ABSTRACT

Vegetation plays an important role in the climate system. The extent to which vegetation impacts climate through its structure and function varies across space and time, and it is also affected by land cover changes. In areas with both multiple growing periods and significant land cover changes, such as the Horn of Africa, identifying vegetation influence on land surface temperature (LST) through radiative changes needs further investigation. In this study, we used a 13-year time series (2001 − 2013) of remotely sensed environmental data to estimate the contribution of radiative mechanism to LST change due to growing season albedo dynamics and land cover conversion. Our results revealed that in taller woody vegetation (forest and savanna), albedo increases during the growing period by up to 0.04 compared with the non-growing period, while it decreases in shorter vegetation (grassland and shrubland) by up to 0.03. The warming impact due to a decrease in albedo during the growing period in shorter vegetation is counteracted by a considerable increase in evapotranspiration, leading to net cooling. Analysis of land cover change impact on albedo showed a regional annual average instantaneous surface radiative forcing of $-0.03 \pm 0.02\,W\,m^{-2}$. The land cover transitions from forest to cropland, and savanna to grassland, displayed the largest mean albedo increase across all seasons, causing an average instantaneous surface radiative forcing of $-2.6\,W\,m^{-2}$ and $-1.5\,W\,m^{-2}$ and a decrease in mean LST of 0.12 K and 0.09 K, all in dry period (December, January, February), respectively. Despite the albedo cooling effect in these conversions, an average net warming of 1.3 K and 0.23 K was observed under the dominant influence of non-radiative mechanisms. These results show that the impact of radiative mechanism was small, highlighting the importance of non-radiative processes in understanding the climatic impacts of land cover changes, as well as in delineating effective mitigation strategies.

1. Introduction

Vegetation impacts climate through its influence on water, energy, and gas exchange between the land surface and atmosphere (Bonan, 2008; Davin and de Noblet-Ducoudre, 2010). The degree to which vegetation impacts climate depends on the type of vegetation and season, and it is affected by land cover changes caused by human perturbations. Hence, improving our understanding of the role of vegetation dynamics in ecosystem processes is crucial for delineating effective mitigation strategies against climate change.

Seasonal changes in vegetation structure (e.g., leaf area index (LAI) and canopy height) and physiology (e.g., photosynthesis and transpiration) affect the surface biophysical properties (albedo, canopy conductance, and surface roughness length), which directly impact the surface energy balance, net radiation partitioning (Pielke et al., 1998; Moore et al., 1996; Richardson et al., 2013), and hence land surface temperature (LST) (Schwartz, 1992). Climate patterns, on the other hand, directly affect vegetation phenology and temporal patterns of ecosystem functioning. The interacting mechanisms and feedbacks of these processes across different ecoregions are not yet fully understood, particularly in remote regions, where observation data on key climate and biophysical variables are scarce. For instance, in the Horn of Africa, the dominating bimodal rainfall pattern, associated with the Inter-tropical Convergence Zone (ITCZ), often results in multiple vegetation

* Corresponding author at: Department of Geosciences and Geography, University of Helsinki, P.O. Box 68, FI-00014, Finland.
E-mail address: temesgen.abera@helsinki.fi (T.A. Abera).

https://doi.org/10.1016/j.rse.2018.11.024
Received 12 June 2018; Received in revised form 6 November 2018; Accepted 17 November 2018

growing periods (Nicholson, 2017). This pattern influences the role of vegetation phenology in regulating the radiation balance and LST through their effect on albedo seasonality.

Previous ground-based albedo measurements in grasslands (Song, 1999), bushlands (Allen et al., 1994), shrublands (Williamson et al., 2016), and forests (Hollinger et al., 2010; Moore et al., 1996) have shown that the albedo of a vegetated surface is strongly affected by phenology. Soil moisture content can also influence the observed seasonal variations in albedo over vegetated surfaces (Allen et al., 1994). Furthermore, other factors not related to the land surface, such as solar zenith angle (SZA) variations, have an impact on the seasonal course of albedo (Song, 1999). However, the extent to which such albedo dynamics affects seasonality of the radiation regime, and how it is partitioned to determine the residual energy available to warm the land surface need further investigation.

Land cover changes also affect the energy balance and LST through modification of surface biophysical properties, particularly albedo, surface roughness and evapotranspiration (ET) (Pielke Sr et al., 1998; Lee et al., 2011; Li et al., 2015; Alkama and Cescatti, 2016). Changes in the net radiation balance of the Earth due to anthropogenic perturbations (e.g., changes in land cover, aerosols, and greenhouse gas concentrations) or natural variability (e.g., solar irradiance and volcanic eruptions) are commonly known as radiative forcing (Myhre et al., 2013). When land cover changes result in the replacement of a darker surface in favor of a brighter one (e.g., in the case of tropical forests being replaced by brighter background soil during deforestation), albedo tends to increase, resulting in negative radiative forcing (Henderson-Sellers and Wilson, 1983; Betts and Ball, 1997). On the other hand, when the conversion happens from a brighter to darker surface (e.g., through afforestation), albedo decreases, resulting in positive radiative forcing.

Although the radiative impact of land cover changes at a global level is the least uncertain of all anthropogenic forcings, the best estimate of $-0.2 \pm 0.2\,W\,m^{-2}$ for pre-industrial times has been produced by climate models (Myhre et al., 2013). Recent studies based on Moderate Resolution Imaging Spectroradiometer (MODIS) data, however, have given smaller estimates ($-0.09\,W\,m^{-2}$) and it has been argued that the radiative impact could have been previously overestimated (Myhre et al., 2013). The wide range in global radiative forcing estimates arises from uncertainties in accurately measuring albedo and land cover changes. Although the impact of land cover change on air temperature and LST has been much studied at a global scale (refer to Perugini et al. (2017) for an extensive literature review), relatively few studies have examined the impacts of individual radiative (albedo) and non-radiative (surface roughness and evapotranspiration) processes using either modeling (Davin and de Noblet-Ducoudre, 2010) or observations (remote sensing and in situ) (Luyssaert et al., 2014; Lee et al., 2011; Bright et al., 2017; Peng et al., 2014). Davin and de Noblet-Ducoudre (2010) have shown that surface albedo change due to global-scale replacement of forest by grassland could cause -1.36 K cooling globally, whereas non-radiative process could cause warming of up to 0.24 K via ET and 0.29 K via surface roughness reductions. Hence, further studies at a global or regional level are still needed in the areas that have undergone significant land cover changes.

This is the case in East Africa, which has faced considerable anthropogenic pressure and land cover conversions due to rapid agricultural expansion over the recent decades. It has been estimated that the region lost about 28% of its natural vegetation at an annual rate of 1.4% between 1990 and 2010 (Brink et al., 2014). The rate varies inside the Horn of Africa; for example, in the Taita Hills in Kenya, 18% of the natural vegetation was lost for cropland between 1987 and 2011 (Pellikka et al., 2018). Given the region's vulnerability to environmental change due to an economy largely dependent on agriculture, such changes in the land surface are likely to amplify climate change impacts, and hence it is important to know how recent land cover conversions are contributing to the local and regional radiative forcing, as well as their corresponding impact on LST.

While most model- and observation-based studies have so far emphasized idealized scenarios of land cover change, for instance through comparing paired sites having contrasting land cover types (i.e., forest versus cropland/grassland), some studies have shown the actual impact of land cover changes on total surface (air) temperature using observation data (e.g., Alkama and Cescatti, 2016; Li et al., 2016). In these studies, however, the relative contribution of individual radiative and non-radiative components to the total temperature change has not yet been fully addressed, given limited ground data availability across space and time. In this regard, remote sensing combined with climate data can provide better spatial and temporal coverage, contributing to more detailed assessments in regions with limited ground data as well as larger-scale studies. Thus, further examination using relatively high resolution remote sensing observations is needed, in the areas that have undergone land cover changes, to better understand the relative contribution of various land cover conversion classes to LST through radiative and non-radiative mechanisms, and to clarify how their impact varies across seasons.

The objective of this study was to clarify the impact of albedo change (radiative change) on radiation balance and LST across the seasonal vegetation growth cycle and due to changes in land cover in the Horn of Africa. Specifically, we analyzed: (1) how vegetation growing season albedo dynamics impacts the local energy balance and LST in four natural vegetation classes: forest, savanna, grassland, and shrubland, and (2) how land cover change affects surface albedo, radiative forcing, net LST change, and the contribution of radiative changes to the LST change and its seasonal variation in the Horn of Africa between 2001 and 2013.

2. Study area

The study area comprises five countries in East Africa: Ethiopia, Kenya, Somalia, Eritrea, and Djibouti (Fig. 1). This region, commonly known as the Horn of Africa, has a great variation in climate, topography, and vegetation. The region is characterized by a semi-arid to arid climate with a dominantly bimodal rainfall pattern. Much of the region receives its main rainfall from March to May and has a short period of rain from October to December. Although the rainfall maxima occur in these seasons, there is a third maximum in July to August in parts of Ethiopia. The seasonal rainfall pattern in the region is largely influenced by the north–south movement of the ITCZ and has significant inter- and intra-annual variations under the impact of the El Niño-Southern Oscillation, the Indian Ocean Dipole (Ogallo, 1988; Nicholson, 1996; Indeje et al., 2000), and the Madden-Julian Oscillation (Nicholson, 2017). Annual rainfall distribution is also influenced by the large elevation differences, which range from 125 m above sea level at the Danakil Depression in Ethiopia to 5199 m above sea level at Mount Kenya and can vary from less than 200 mm in the lowlands to more than 1500 mm in the highlands (Fig. 1b). Annual average temperature is considerably different between the lowland desert areas, where it can soar up to 34 °C at the Danakil Depression, and the highland forests, where it can drop as low as 12 °C (Fig. 1c).

Associated with its climatic and topographic diversity, the region is endowed with multiple ecoregions (Sudanian, Somali-Masai, Zanzibar-Inhambane regional mosaic, and Afromontane). The Sudanian ecoregion extends up to the foothills of the Ethiopian highlands in the western parts of the study area, which is comprised of mainly woodlands and is indicated as wooded savanna in Fig. 1d. The Somali-Masai ecoregion occupies a large portion of the study region (including southern and eastern Ethiopia, and much of Kenya and Somalia) and contains mainly shrubland, bushland, thicket, and grassland. The Zanzibar-Inhambane ecoregion covers a small area in the southern periphery of Somalia and the eastern-most parts of Kenya and comprises shrubland, thicket, wooded grassland, and scrub forest. The Afromontane ecoregion occupies the highlands of Ethiopia and Kenya and

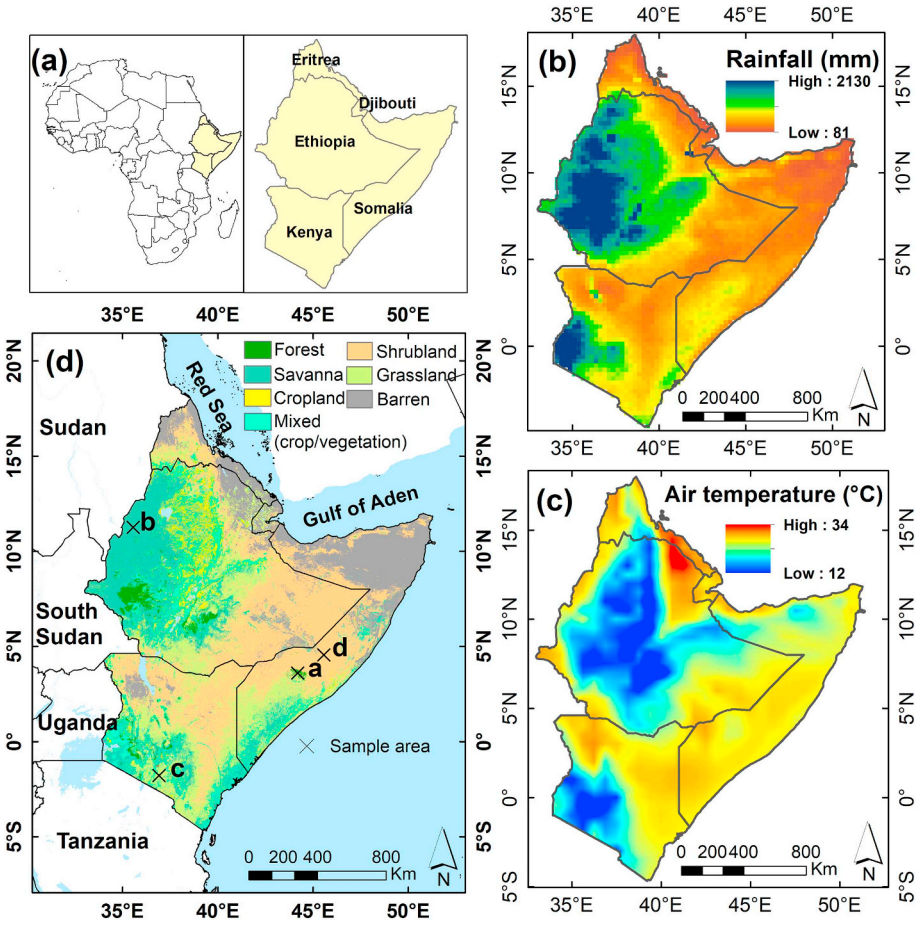

Fig. 1. Location of the study area with: (a) map of the study area, (b) annual average rainfall from the Tropical Rainfall Measuring Mission (TRMM3B43), (c) annual average air temperature from Modern-Era Retrospective analysis for Research and Applications (MERRA-2), and (d) land cover (MODIS 2001). Sample areas in (d) show locations of stable land cover (3 × 3 km) used for analyzing impacts of vegetation seasonality on albedo, land surface temperature, and energy budget (a = deciduous forest; b = savanna; c = grassland; d = shrubland).

covers only a small area (White (1983) and Fig. 1d).

3. Material and methods

3.1. Remote sensing and meteorological reanalysis data

In this study, we used a large variety of remotely sensed environmental data, including albedo, leaf area index (LAI), LST, emissivity, air temperature, ET, land cover, and surface incoming shortwave radiation (SIS). All the data covered the period between 2001 and 2013, except for LAI (2003 − 2013). For consistent spatial analysis, all products were compared at 1 km spatial resolution. The products with 500 m resolution (LAI and land cover) were aggregated to 1 km to match the resolution of the other products. In aggregating land cover data, the dominant land cover type was assigned for each pixel (i.e., at least three out of the four 500 m pixels should belong to the same class, otherwise were removed from our analysis). Air temperature and SIS data were resampled to 1 km resolution using bilinear interpolation. A summary of the data used in this study is presented in Table 1.

Shortwave broadband black sky albedo (SBSA) (0.3–5.0 μm) at local solar noon was obtained from the MODIS collection 6 MCD43B3 product, at 1 km spatial resolution (NASA LP DAAC, 2016b). Its accuracy is mostly better than 0.05 for SZA below 70° (Liu et al., 2009). We chose black-sky albedo for this study since it represents albedo at local noon and is consistent in time with empirical model used in this study (e.g. Eq. (9)). Furthermore, black-sky, white-sky, and blue-sky albedo are so strongly correlated in the region that the selection of albedo type does not affect the results (Supplementary Fig. S1a, b) (Li et al., 2015).

LAI was obtained from the MODIS MCD15A2H product at 500 m resolution, prepared from atmospherically corrected surface reflectance (MOD09) and the revised multiyear land cover product (MCD12Q1) (Myneni et al., 2015). We used the quality flags provided with the product to select only the best quality retrievals based on the main radiative transfer method without saturation (Yang et al., 2006).

Table 1
Remote sensing and meteorological reanalysis data.

Data type	Sensor	Product	Version	Spatial resolution	Temporal resolution	Year	Reference
BRDF/Albedo model parameters	MODIS	MCD43B1	5	1 km	8-Day composite	2001–2013	NASA LP DAAC, 2014
LST	MODIS	MOD11A2	6	1 km	8-Day composite	2001–2013	Wan et al., 2015
Emissivity	MODIS	MOD11B3	6	6 km	Monthly	2001–2013	Wan et al., 2015
Black-sky albedo (BSA)	MODIS	MCD43B3	6	1 km	8-Day composite	2001–2013	NASA LP DAAC, 2016b
Leaf area index	MODIS	MCD15A2H	6	500 m	8-Day composite	2003–2013	Myneni et al., 2015
Evapo-transpiration	MODIS	MOD16A2	6	1 km	8-Day composite	2001–2013	Running et al., 2017
Land cover	MODIS	MCD12Q1	051	500 m		2001–2013	NASA LP DAAC, 2016a
Air temperature		MERRA-2		0.5° × 0.6°	Monthly	2001–2013	GMAO, 2015
Surface Incoming Shortwave Radiation (SIS)	MVIRI/SEVIRI	Heliosat (SARAH)	2	0.05°	Monthly	2001–2013	Pfeifroth et al., 2017
Precipitation	TRMM	TRMM 3B43	7	0.25°	Monthly	2001–2013	GES DISC, 2016

The product used for LST was the MOD11A2, which provides 8-day average radiometric temperature for clear-sky conditions at 1 km resolution (Wan et al., 2015). To ensure the use of only high-quality and cloud-free pixels, we used quality assessment flags to filter valid LST pixels using quality control flag bits with a value of zero. Previous studies indicate that this product has an accuracy better than 1 K over vegetation, soil, and lakes (Wan et al., 2015).

Estimates of ET were obtained from the MOD16A2 gap-filled product at 1 km resolution (Running et al., 2017). This product is based on the Penman-Monteith equation, daily meteorological data (air temperature, surface downward solar radiation, vapor pressure deficit, wind speed, and relative humidity), and MODIS 8-day albedo, LAI, and land cover data. It has a mean absolute error of around 0.3 mm day^{-1} when compared with eddy flux towers (Running et al., 2017).

Land cover was mapped using the collection 051MCD12Q1 product at 500 m resolution (NASA LP DAAC, 2016a). The product has an overall accuracy of around 75% (Friedl et al., 2010). We used the International Geosphere-Biosphere Programme (IGBP) type 1 classification schemes in our study.

Air temperature was obtained from the Modern-Era Retrospective analysis for Research and Applications (MERRA-2) monthly product at 0.5° × 0.6° resolution (GMAO, 2015). MERRA-2 is a screen-level (2 m) air temperature reanalysis product derived from combined satellite and weather data by the Global Modeling and Assimilation Office (GMAO) in the USA. Evaluation of the product with in situ data over land surfaces showed a daily mean bias of 0.1 K and daily maximum bias of 1.5 K (Michael et al., 2015).

Monthly SIS, at 0.05° resolution, was obtained from the satellite-based climate data record for the all-sky condition, derived from satellite observations of the visible channels of the MVIRI and the SEVIRI instruments onboard the geostationary Meteosat satellites (Pfeifroth et al., 2017). Several input data from satellite (e.g., effective cloud albedo from Meteosat and surface albedo for the clear-sky model from SARB/CERES), ERA-Interim reanalysis data (e.g., monthly mean total water vapor and ozone), European Centre for Medium-Range Weather Forecasts data (ECMWF) (e.g., aerosol optical thickness), and lookup tables based on the radiative transfer model were used for preparing the SIS product. Validation of monthly mean SIS against reference ground measurements of the Baseline Surface Radiation Network (BSRN) showed a mean absolute bias of around 5 W m^{-2} (Pfeifroth et al., 2017).

Precipitation data was obtained from the Tropical Rainfall Measuring Mission (TRMM) at 0.25° spatial resolution. The product (TRMM 3B43 version 7) combines the 3-hourly merged infrared estimates from the monthly accumulated Global Precipitation Climatology Centre (GPCC) rain gauge analysis (GES DISC, 2016).

3.2. Identifying impact of vegetation seasonality on albedo, land surface temperature, and energy budget

To identify the effects of vegetation seasonality on albedo and LST, 3 × 3 km sample areas were selected from savanna, grassland, shrubland, and forest, as they are the dominant natural vegetation cover types in the region. As evergreen forest showed non-significant relationship with LAI seasonality in the region, we selected deciduous forest for our analysis (Supplementary Fig. S2). In selecting samples, only stable area was used from each biome. To identify stable areas, the 13 land cover layers (2001–2013) were first spatially stacked and the frequencies of all the land cover categories (i.e., the number of occurrences) were calculated for each pixel. Next, a frequency map was generated using the highest frequency value for each pixel. Hence, if a pixel did not experience any land cover changes during 2001–2013 (i.e., land cover was stable), the maximum frequency was equal to 13. Through this process, a representative 3 × 3 km area was chosen from each of the four stable classes (Fig. 1d). To establish a reliable relation between LAI and albedo for a specific land cover type, it is important to avoid mixing of land cover types by selecting stable pixels throughout the time series (2001–2013). This limits the flexibility of choosing multiple samples particularly in case of grassland and shrublands. In savannas, however, where there are more stable samples in the region, multiple sites were tested to cross-check the result (Fig. S3).

Vegetation and albedo seasonal variations were inferred using climatologies of 8-day composite LAI and SBSA from MODIS data for the four stable areas. First, average LAI for each 8-day period was calculated for the years 2003–2013. Data for 2001 and partly 2002 were not available and were hence considered missing in 8-day average LAI computation. Then, the 8-day average seasonal albedo changes were computed from SBSA likewise and plotted against LAI for the four land cover classes (forests, grassland, savanna, and shrubland). Furthermore, as albedo varies seasonally with SZA, SBSA at constant SZA (= 30°) was calculated (Schaaf et al., 2002) for the year 2003, using MCD43B1 albedo model parameter, to check its difference compared with the MCD43B3 albedo product, which represents instantaneous albedo at local noon. The comparison showed that the difference between SBSA at constant SZA and local noon is small (Supplementary Fig. S4), and SBSA at local noon can be used.

To check the robustness of MODIS albedo seasonality data, we carried out the same analysis using a different SBSA data source from the Global LAnd Surface Satellite (GLASS) project (Liang and Liu, 2012). The GLASS SBSA product that we used has the same temporal and spatial resolution as MODIS MCD43B3. It also uses MODIS data as input but has a different algorithm for calculating albedo. Comparison of the two data sources gave similar results (Supplementary Fig. S5). Moreover, to assess the spatio-temporal correlation between LAI and albedo across the whole study region, a non-parametric Spearman correlation was calculated using monthly climatologies for 2001–2013.

The impact of phenology-induced albedo dynamics on net shortwave radiation was estimated using Equation

$$\Delta S_{(\alpha)} = SW_{in} * \Delta\alpha \quad (1)$$

where $\Delta S_{(\alpha)}$is the change in net shortwave radiation due to albedo dynamics; SW_{in} is the monthly incoming shortwave radiation (here we used constant SW_{in} from monthly climatology to determine the impact due to albedo dynamics only); $\Delta\alpha$ is the maximum albedo change between the growing and non-growing season. Growing season, in this paper, refers to the period of the year during which the local weather conditions (temperature, sunlight, and rainfall) are adequate for plant growth and this includes the canopy development from leaf-out to green-up. The region has multiple growing seasons that follow the rainfall modality patterns, which vary spatially and temporally across the region (Abera et al., 2018).

The seasonal relations of LST, SBSA, ET, and SIS data were assessed using 2001–2013 monthly climatologies. First, good quality pixels were filtered using quality flags and then all 8-day composite data were temporally aggregated to monthly time-scale before computing climatologies. As LST, SBSA, and ET are 8-day composite data, the monthly aggregation is temporally synchronous. But for the SIS data, which are available at daily and monthly scale, we chose the monthly data since its accuracy is better than the daily data (Pfeifroth et al., 2017). Spearman correlation was first used to assess the relationship between monthly climatologies of SBSA and LST, and ET and LST. Then, the monthly impact of albedo on net shortwave radiation and the residual available energy for heating the land surface was calculated using Eqs. (2) and (3), respectively:

$$SW_{net(i)} = SW_{in(i)} - SW_{out(i)} = (1 - \alpha_{(i)}) * SW_{in(i)} \quad (2)$$

where $SW_{net(i)}$ is the monthly net shortwave radiation (W m^{-2}); SW_{in} is the monthly incoming shortwave radiation (W m^{-2}); α is the monthly albedo; SW_{out} is the monthly outgoing shortwave radiation (W m^{-2}); i is the month (i = 1–12).

$$RE_{(i)} = SW_{net(i)} - ET_{(i)} \quad (3)$$

where $RE_{(i)}$is the monthly available residual energy for heating the land surface, and $ET_{(i)}$ is the monthly ET in $W\,m^{-2}$ ($1\,mm\,day^{-1} = 28.36\,W\,m^{-2}$; $1\,mm\,day^{-1} = 2.45\,MJ\,m^{-2}\,day^{-1}$; $1\,W\,m^{-2} = 0.0864\,MJ\,m^{-2}\,day^{-1}$).

3.3. Biophysical effects of land cover changes on albedo, radiative forcing, and land surface temperature

To identify land cover changes, stable land cover maps representing initial and final conditions were prepared using the MODIS 2001–2013 product. First, the initial (2001–2005) and final (2009–2013) five years were used to identify the most frequent land cover type in each pixel following the same approach as described in Section 3.2. Only pixels in which land cover was stable for at least three years were used, while pixels below this threshold were removed. By this process, from the original 2,480,737 pixels (excluding water bodies), 67,140 (2.70%) and 66,053 pixels (2.66%) were removed from the initial and final land cover maps, respectively. Then, land cover change pixels were identified by comparing the two maps. The idea was to minimize the impact of land cover classification errors on our land cover change estimation by identifying changes only in stable pixels between the initial and final five years.

To know the impact of land cover changes on albedo, we compared the average albedo of the first and last five years, which represents the initial (2001–2005) and final conditions (2009–2013) for each land cover change pixel, respectively. Then, the impact of shortwave albedo change on the surface radiation was estimated from instantaneous shortwave surface radiative forcing (ISRF) using Eq. (4):

$$ISRF = -SW_{in} * (\alpha_f - \alpha_i) \tag{4}$$

where $SW_{in}$is incoming shortwave radiation, and α_i and α_f are albedo before and after the change, respectively.

The regional instantaneous shortwave surface radiative forcing (RISRF) was estimated from the individual land cover change contributions using Eq. (5) (Bright, 2015; Jin & Roy, 2005):

$$RISRF = \sum_{i=1}^{7}\left(ISRF_i * \frac{A_i}{A_t}\right) \tag{5}$$

where $ISRF_i$ is the instantaneous shortwave surface radiative forcing for land cover change (i); A_i is the land surface area covered by land cover change i; A_t is the total land surface area of the study region ~2,480,737 km^2; i (land cover change codes) = 1–7: grassland to shrubland = 1; shrubland to grassland = 2; savanna to mixed = 3; grassland to savanna = 4; savanna to cropland = 5; savanna to grassland = 6; forest to cropland = 7.

For estimating the contribution of radiative mechanisms to LST shift due to albedo changes associated with land cover change, we used an analytical expression based on the energy balance approach initially proposed by Lee et al. (2011):

$$\Delta T_s = \frac{\lambda_0 * \Delta S}{(1+f)} + \frac{(-\lambda_0) * R_n * \Delta f}{(1+f)^2} \tag{6}$$

where $\Delta T_s$is the calculated surface temperature change; ΔS is the net shortwave radiation change; f is the monthly mean energy redistribution factor; Δf is the change in energy redistribution due to land cover change;R_n is the monthly mean net radiation; $\lambda_0$is the 2001–2013 monthly mean temperature sensitivity from the longwave radiation feedback ($K\,(W\,m^{-2})^{-1}$).

The first term on the right-hand side of Eq. (6) represents the temperature change due to the radiative mechanism and the second term shows the remaining impact from the non-radiative mechanisms (evapotranspiration and surface roughness). The $\lambda_0$was computed using Eq. (7).

$$\lambda_0 = \frac{1}{4 * e_s * \sigma * T_s^3} \tag{7}$$

e_s and $T_s$are 2001–2013 monthly mean surface emissivity and surface temperature (K), respectively; σ is the Stefan-Boltzmann constant ($W\,m^{-2}\,K^{-4}$)..

The energy redistribution factor (f) was estimated using Eq. (8) (Lee et al., 2011) from surface and air temperature, net radiation, and ground heat flux (G):

$$f = \frac{\lambda_0}{T_s - T_a}(R_n^* - G) - 1 \tag{8}$$

where $R_n^* \approx R_n$ is the apparent net radiation. G was estimated by multiplying the ratio of G and net radiation (R_n) by R_n. The G/R_n ratio was estimated using an empirical equation by Bastiaanssen (2000), which represents values near local noon:

$$\frac{G}{R_n} = (T_s - 273.15)(0.0038 + 0.0074 * \alpha)(1 - 0.98 * NDVI^4) \tag{9}$$

The SBSA (α) used in this equation represents albedo at local noon and thus is consistent in time with the model. NDVI is the normalized difference vegetation index, which was calculated using surface reflectance imagery obtained from the MODIS albedo model parameter product (MCD43B1), using the following formula: NDVI = (NIR − R) / (NIR + R), where NIR is the near-infrared reflectance and R is the red reflectance. All surface reflectance values were corrected for the sun-sensor geometry (by fixing the view angle at the nadir and the sun angle at 45°) to avoid non-vegetation signals from bidirectional reflectance distribution function (BRDF) effects. Rn was estimated using Eq. (10) (Cleugh et al., 2007):

$$R_n = SW_{in}(1 - \alpha) + \sigma * (e_a - e_s) * T_a^4 \tag{10}$$

$$e_a = 1 - 0.261 * \exp(-7.77 * 10^{-4} * T_a^2) \tag{11}$$

where e_a is air emissivity; T_a is air temperature. In estimating net radiation, we estimated surface emissivity (e_s) from averages of MODIS band 29 (8.40–8.70 μm, in the broadband region), 31 (10.78–11.28 μm), and 32 (11.70–12.27 μm), instead of the average of the emissivities in bands 31 and 32, as doing so could overestimate emissivities in arid and semi-arid regions (Wan et al., 2002). We used the MOD11B3 product, which contains monthly emissivity in band 29 at 6 km resolution, and resampled it to 1 km resolution to match resolutions of bands 31 and 32.

Furthermore, to evaluate the reliability of the partition method, we compared the calculated LST changes (ΔT_s) with the observed LST changes (hereafter $\Delta T_s'$) measured by the MOD11A2 product. To compute $\Delta T_s'$, LST change due to background climate signal was computed and removed from the analysis as follows. First, stable pixels during 2001–2013 were identified using the same methodology as described in Section 3.2. Second, LST changes over the stable pixels were estimated from the slope of a linear regression during 2001–2013. Third, a 9 × 9 km search window was prepared, and mean LST difference due to background climate signals over every target land cover change pixel was estimated from the adjacent stable pixels using the search window (Abera et al., 2018; Alkama and Cescatti, 2016). This approach assumes that pixels within a 9 × 9 km area share the same background climate signals. Finally, we subtracted the background climate signal from the LST difference between the mean LST for the last and the first five years during 2001–2013 over every land cover change pixel.

4. Results

4.1. Impact of vegetation seasonality on albedo, land surface temperature, and energy budget

In forest and savanna, albedo increased during the vegetation growing period (Fig. 2a, b). In forest, BSA increased by 8%, and in savanna it increased by 27%, between winter minima and growing season maxima. Both displayed an offset with LAI seasonality in the

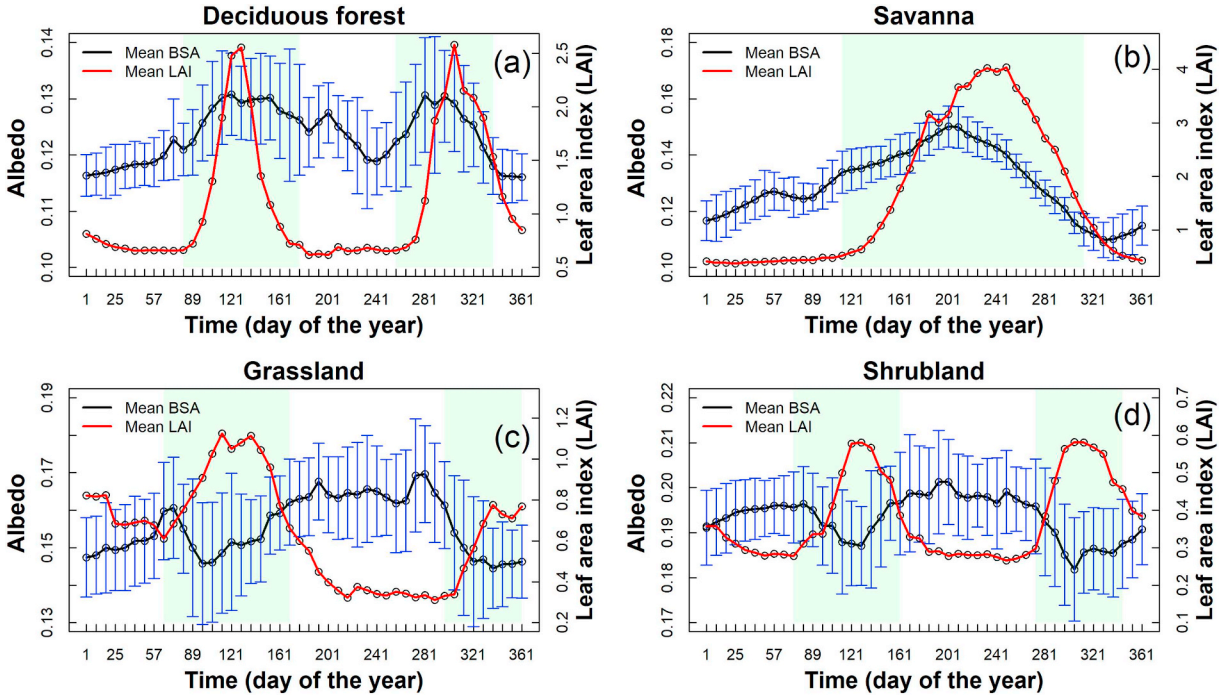

Fig. 2. Seasonality of average 8-day composite leaf area index (LAI) and shortwave broadband black sky albedo (SBSA) over 2001–2013 in the Horn of Africa in (a) deciduous forest, (b) savanna, (c) grassland, and (d) shrubland. The same sample size (3 × 3 km) was used for each ecoregion from stable areas (see Fig. 3d). Error bars show mean ± standard deviation of SBSA. Shaded area shows growing period.

Table 2
Qualitative metrics on impact of growing period albedo dynamics on net shortwave radiation.

Land cover	α_{gs}	α_{ng}	$\Delta\alpha$	$\Delta S_{(\alpha)}$(W m^{-2})
Forest	0.13	0.12	0.01 (8%)	−2.47
Savanna	0.15	0.11	0.04 (27%)	−10
Grassland	0.14	0.17	−0.03 (18%)	7.11
Shrubland	0.18	0.20	−0.02 (10%)	5.04

α_{gs} = growing season albedo; α_{ng} = non-growing season albedo; $\Delta\alpha$ = albedo change; $\Delta S_{(\alpha)}$ = net shortwave radiation changes due to albedo dynamics.

growing period (i.e., albedo reached a peak value before LAI by up to two weeks in forest and four weeks in savanna, and sharply decreased afterwards). The albedo increments in forest and savanna, during the growing period, caused a $-2.47\ W\,m^{-2}$ and $-10\ W\,m^{-2}$ decrease in available energy, respectively (Table 2). Additional analysis using multiple stable samples in savanna showed similar increasing patterns in albedo during the growing season (Fig. S3).

In grassland and shrubland, albedo and LAI had opposite seasonal patterns (Fig. 2c, d). In the growing period, albedo decreased by 18% in grassland and by 10% in shrubland between the maximum and minimum values in winter and the growing season, respectively. The negative relationship between albedo and LAI seasonality had an offset of ~1–2 weeks in grassland and a small offset (~1 week maximum) in shrubland. The decline in albedo during the growing period in grassland and shrubland resulted in a rise in available energy of $7.11\ W\,m^{-2}$ and $5.04\ W\,m^{-2}$, respectively (Table 2).

The Spearman correlation between albedo and LAI seasonality across the study region showed a similar pattern, i.e., deciduous forest and savanna displayed a mainly positive correlation ($r > 0.7$), while shrubland and grassland had mostly a negative correlation ($r < -0.8$) in the areas of a statistically significant albedo-LAI relation (Fig. 3a). With LST, on the other hand, albedo indicated an opposite relation to that of the albedo-LAI correlation for most parts of land cover classes of significant ($P < 0.05$) relation (Fig. 3b). In other words, albedo had a negative correlation with LST in deciduous forest and savanna, while it had a positive correlation in shrubland and grassland in areas of a significant albedo-LST relation. However, albedo and LST dominantly had a non-significant ($P > 0.05$) relation for large parts of the study region.

Hence, depending on land cover type, we observed an opposite relationship between LST and albedo in areas of significant relation. To understand the factors driving these discrepancies, we analyzed how ET (latent heat flux) correlates with LST across the same areas (Fig. 3c). The result showed that ET had a negative correlation with LST ($r < -0.6$) in all regions, independently of the characteristics of the relationship (positive or negative) between albedo and LST. A multiple regression model using LST, ET, and albedo was assessed to further evaluate the interaction between these variables. The multiple regression result confirmed a consistent negative relation between ET and LST across the region, although the influence of albedo in driving LST variability was not significant ($P > 0.05$) (Fig. S6). These results indicate that the positive relationship between LST and albedo observed in most regions is not causal but is instead heavily determined by the effects of ET on LST patterns.

Furthermore, to demonstrate the seasonal dynamics of net shortwave and residual energy distribution over such areas, where an opposite relationship between LST and albedo was observed, we selected two samples: one from areas with positive LST–albedo and the other from negative LST–albedo seasonality correlations (see Fig. 3b for location of samples S1 and S2).The results showed that in the areas where LST–albedo had a negative relation, net shortwave radiation and residual energy had a positive relation (Fig. 4a). Between March and July, when a maximum 11 °C fall in LST was observed, albedo increased by 33% (0.035), ET increased by 81% ($4.1\ mm\ day^{-1} \approx 116\ W\,m^{-2}$), and net shortwave radiation and residual available energy reduced by 23% ($51\ W\,m^{-2}$) and 87% ($167\ W\,m^{-2}$), respectively. Much of the energy was used for ET ($116\ W\,m^{-2}$) between March and July, which follows the precipitation pattern.

In the areas where LST–albedo had a positive relation, net shortwave radiation showed a positive relation except in the wet period

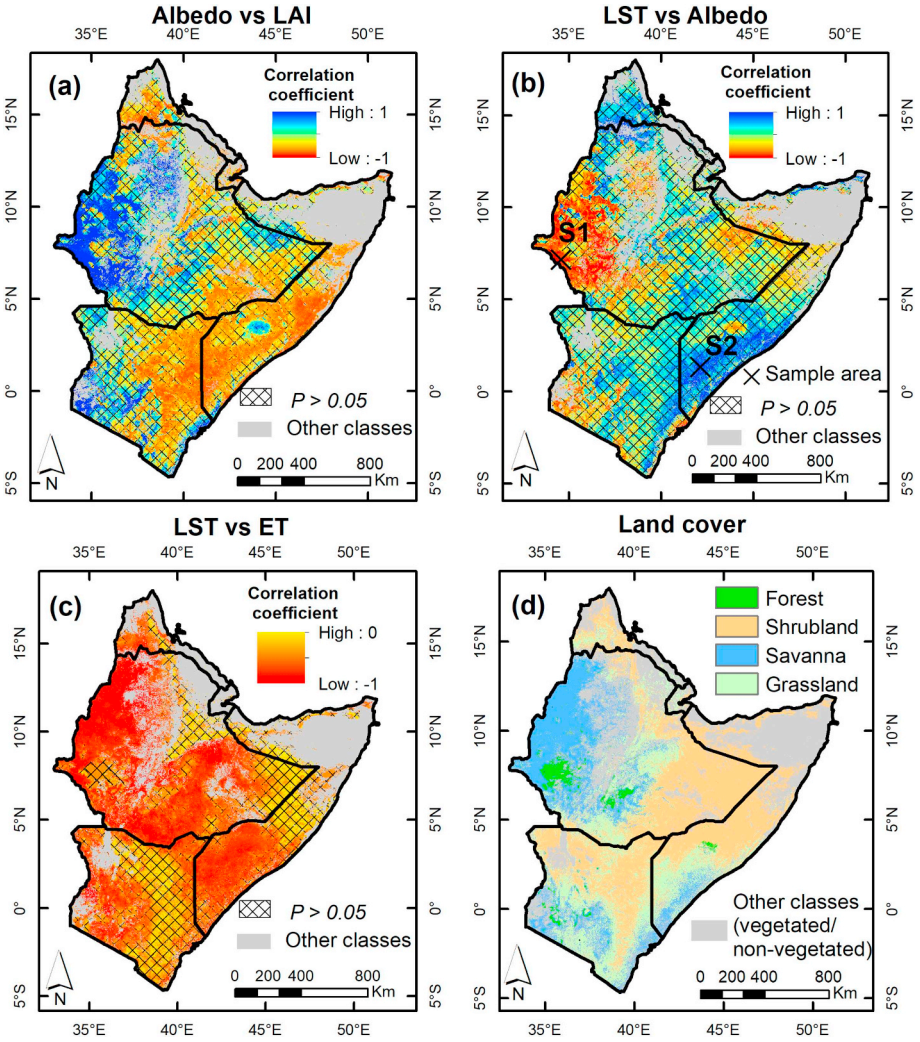

Fig. 3. Seasonality correlation of monthly average: (a) albedo and leaf area index (LAI), (b) land surface temperature (LST) and albedo, and (c) LST and evapotranspiration (ET) in the Horn of Africa between 2001 and 2013. Statistically non-significant correlations are marked with hashes. Panel (d) shows International Geosphere-Biosphere Programme (IGBP) classes: forest (evergreen and deciduous), shrubland (open and closed), savanna (wooded savanna and savanna), and grassland. All other classes are masked in all panels.

(October and November), while residual energy displayed positive relation across all seasons (Fig. 4b). When LST dropped by a maximum of 13 °C between September and November, albedo decreased by 14% (0.03), whereas net shortwave radiation increased by 3.6% (7.4 W m^{-2}). For the same period, residual energy on the contrary dropped by 18% (31 W m^{-2}) for the corresponding increase in ET of > 100% (1.34 mm day^{-1} ≈ 38 W m^{-2}).

4.2. Impact of land cover changes on albedo, radiative forcing, and land surface temperature

From the total land area of the study region (2,480,737 km^2) around 5% (128,249 km^2) experienced land cover changes between 2001 and 2013 (Fig. 5). Of these, grassland to shrubland and savanna to mixed (crop/vegetation) conversions made up 58% of the total land cover change. The remaining land cover changes consisted of shrubland to grassland (15%), grassland to savanna (10.6%), savanna to grassland (8.3%), savanna to cropland (7.2%), and forest to cropland (1.3%) conversions (Table 3).

Taller to shorter vegetation conversions (i.e., forest to cropland, savanna to grassland, and savanna to mixed crop/vegetation) all displayed consistent mean albedo increase in all seasons. The largest increase was observed in December, January, February (DJF), while the smallest was in September, October, November (SON) in all conversions. In terms of magnitude of change, forest to cropland conversion displayed the biggest mean albedo increase at 0.01 (SD 0.009), followed by savanna to grassland (mean 0.006 and SD 0.007), and savanna to mixed (crop/vegetation) (mean 0.003 and SD 0.005) conversions (Fig. 6). These conversions generated a corresponding mean ISRF of −2.6 W m^{-2}, −1.5 W m^{-2}, and − 0.8 W m^{-2} (Fig. 6) and a subsequent average LST cooling of −0.12 K, −0.09 K, and − 0.04 K, respectively, all during DJF (Fig. 7a). Despite the cooling by radiative mechanisms, these conversions generated a substantial and consistent warming of 1.66 K, 0.58 K, and 0.57 K, respectively, from the non-radiative mechanisms (Fig. 7b). Contrary to the rest of taller to shorter vegetation conversions, savanna to cropland conversion exhibited inconsistent patterns across seasons in all physical parameters (i.e., albedo, radiative forcing, and LST change) (Figs. 6–8).

In land cover changes occurring in shorter vegetation types, grassland to shrubland and grassland to savanna showed relatively small yet consistent rise in albedo in all seasons (Fig. 6). The maximum average albedo change was in DJF and the minimum in SON for both conversions. The maximum mean albedo increase of 0.005 (SD 0.008) in grassland to shrubland and a mean of 0.003 (SD 0.006) in grassland to savanna conversions resulted in an average ISRF of −1.38 W m^{-2} and −0.8 W m^{-2} (Fig. 6), and a LST cooling of −0.08 K and − 0.04 K,

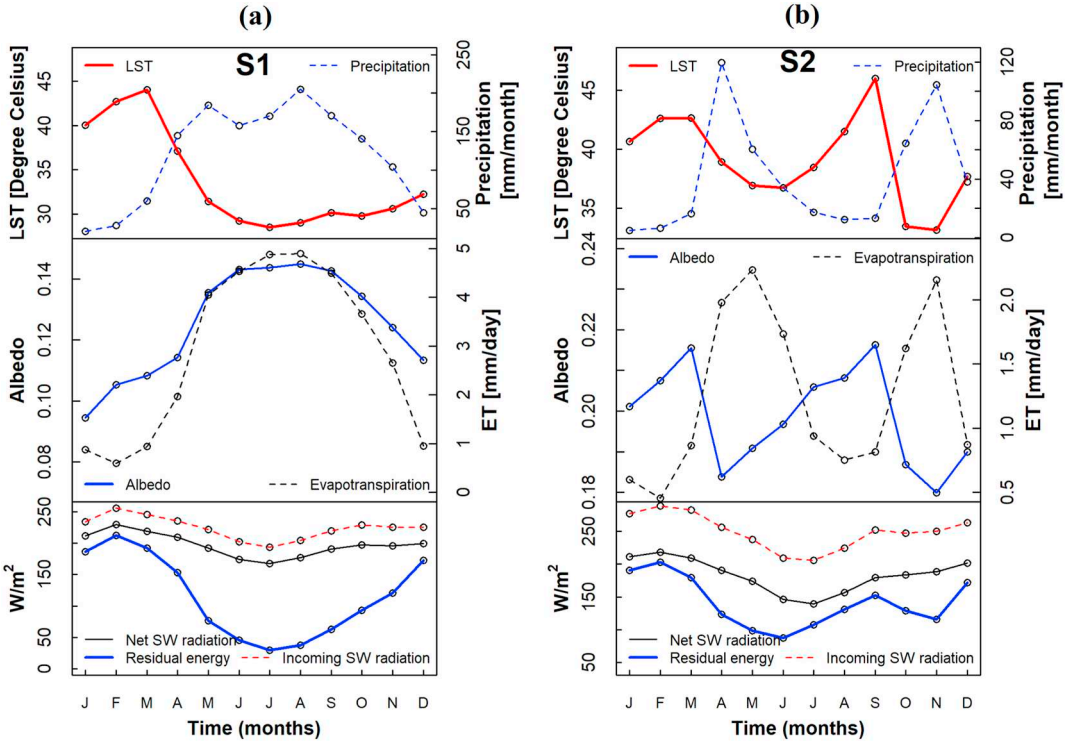

Fig. 4. Seasonality of land surface temperature (LST), precipitation, net shortwave (SW) radiation, and residual energy for areas where albedo and evapotranspiration (ET) had: (a) positive relation in sample site S1 and (b) negative relation in sample site S2. Residual energy calculated from net SW radiation minus evapotranspiration. Sample sites S1 and S2 (3 × 3 km each) were selected from stable areas in savanna and grassland where albedo had strong negative ($r < -0.8$) and positive ($r > 0.8$) correlations with LST respectively (see Fig. 3b for location of the sample sites).

respectively (Fig. 7b), whereas the corresponding ΔT_s due to non-radiative mechanisms showed inconsistent pattern across seasons (Fig. 7a). In shrubland to grassland conversions, on the other hand, mean albedo showed a very small and inconsistent variation across seasons (i.e. albedo increased by 0.002 in DJF; decreased by the same magnitude (−0.002) in SON); and displayed a relatively small increase in June, July, August (JJA) (mean 0.0002) and March, April, May (MAM) (0.0007) (Fig. 6). The DJF and SON albedo change has a

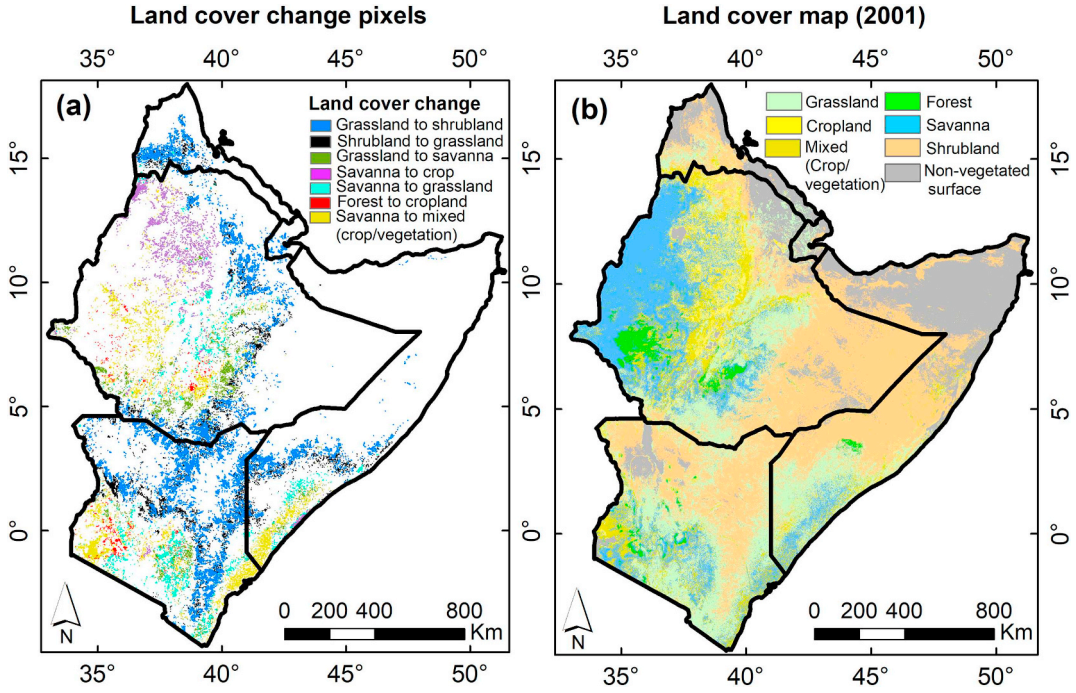

Fig. 5. Map showing (a) land cover change pixels identified by comparing the most frequent land cover type in each pixel during the first and last 5 years of the study period (2001–2013), and (b) Moderate Resolution Imaging Spectroradiometer (MODIS) 2001 land cover map. Only land cover change pixels ≥2 km^2 were considered.

Table 3
Land cover conversions and their areas.

Conversion type	Area (km^2)	Percentage of the total change (%)
Grassland to shrubland	47,881	37.3
Savanna to mixed (crop/vegetation)	26,046	20.3
Shrubland to grassland	19,202	15
Grassland to savanna	13,580	10.6
Savanna to grassland	10,634	8.3
Savanna to cropland	9249	7.2
Forest to cropland	1657	1.3
Total area	**128,249**	

radiative forcing of $-0.4\ W\ m^{-2}$ and $0.4\ W\ m^{-2}$, respectively (Fig. 6). The DJF albedo-increase caused -0.03 K cooling while the SON albedo-reduction brought warming of same magnitude (Fig. 7b). Similar inconsistent patterns *in* ΔT_s were exhibited by the non-radiative mechanisms across seasons (i.e. cooling in DJF and warming in SON by the same magnitude) in shrubland to grassland conversions (Fig. 7a).

The average RISRF estimated from the relative contribution of each land cover conversion class showed negative forcing and considerable variation across seasons. The maximum mean RISRF was in DJF ($-0.056\ W\ m^{-2}$) and the minimum in SON ($-0.008\ W\ m^{-2}$). Overall, land cover changes in the region exerted a mean annual RISRF of $-0.03\ W\ m^{-2} \pm 0.02$ (Table 4).

In forest to cropland and savanna to grassland conversions, despite the cooling effect by an increase in mean albedo, the total average $\Delta T_s'$ increased across all seasons, while it fluctuated in savanna to mixed (crop/vegetation) conversions (Fig. 8). Forest to cropland transition exhibited a maximum average LST warming of 1.2 K (in DJF) and a minimum of 0.7 K in SON, whereas savanna to grassland conversion showed an average warming of a maximum of 0.42 K (in MAM) and a minimum of 0.09 K during SON. The average $\Delta T_s'$ in Savanna to mixed (crop/vegetation) conversions, on the other hand, fluctuated (increased during DJF and JJA by the same magnitude (~0.12), and decreased in MAM (-0.31 K) and SON (-0.40 K)). Similarly, savanna to cropland conversion experienced inconsistent $\Delta T_s'$ patterns across seasons.

In shorter vegetation conversions, the average $\Delta T_s'$ fluctuated in grassland to shrubland transitions, whereas it exhibited consistent cooling in grassland to shrubland conversion across seasons, ranging -0.7 K (in MAM) to -0.1 K (SON). Likewise, in grassland to savanna conversion, a consistent decrease in average $\Delta T_s'$ ranging -0.85 K (in MAM) to -0.11 K in DJF, was exhibited across all seasons (Fig. 8).

Comparison of the seasonal average observed $\Delta T_s'$ and calculated LST changes (ΔT_s) (Fig. 8) across biomes had a relatively small difference in regions of land cover conversion from forest to cropland (-0.13 K) and savanna to grassland (-0.19 K). Whereas in grassland to savanna (-0.63 K) and savanna to mixed (crop/vegetation) (-0.49 K) transitions, it had relatively big difference, and hence larger uncertainty. The rest of the land cover conversions had a moderate difference ranging between -0.2 K (in grassland to shrubland) and -0.31 K (in shrubland to grassland and savanna to cropland).

Furthermore, the degree of agreement between $\Delta T_s'$ and ΔT_s across seasons was assessed in a scatterplot (Fig. 9). The result showed that the observed and calculated LST difference had moderate agreement (Fig. 9). The agreement was the best ($r^2 = 0.77$) in the dry season (DJF). Besides, the wet seasons (MAM and SON) demonstrated very similar results ($r^2 = 0.61$ and 0.62), while JJA displayed the lowest agreement ($r^2 = 0.50$), indicating higher uncertainty in the calculated LST changes during this period.

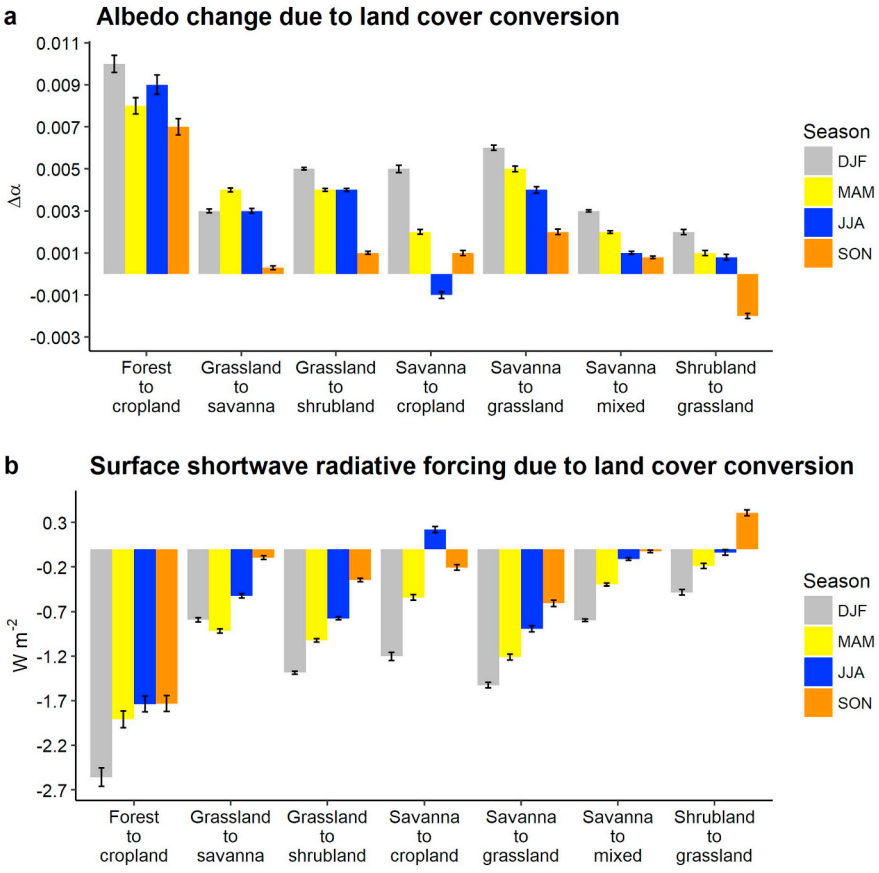

Fig. 6. Seasonal mean albedo change (a) and instantaneous surface radiative forcing (ISRF) (b) associated with land cover conversions during 2001–2013 in the Horn of Africa. All land change pixels were considered for each conversion class in four seasons (DJF, MAM, JJA, and SON). Error bars show the 95% confidence interval. DJF = December, January, February; JJA = June, July, August; MAM = March, April, May; SON = September, October, November.

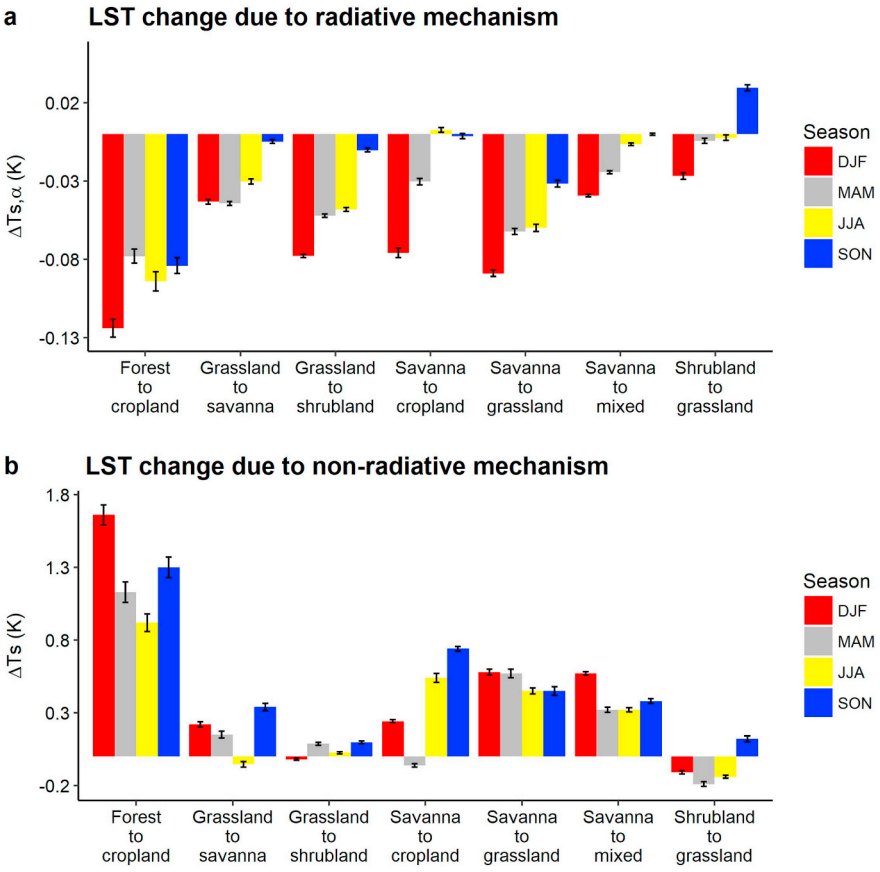

Fig. 7. Contribution to average observed land surface temperature (LST) change by (a) radiative and (b) non-radiative mechanisms following land cover conversions in the Horn of Africa between 2001 and 2005 and 2009–2013 in four seasons. Error bars show the 95% confidence interval. DJF = December, January, February; JJA = June, July, August; MAM = March, April, May; SON = September, October, November.

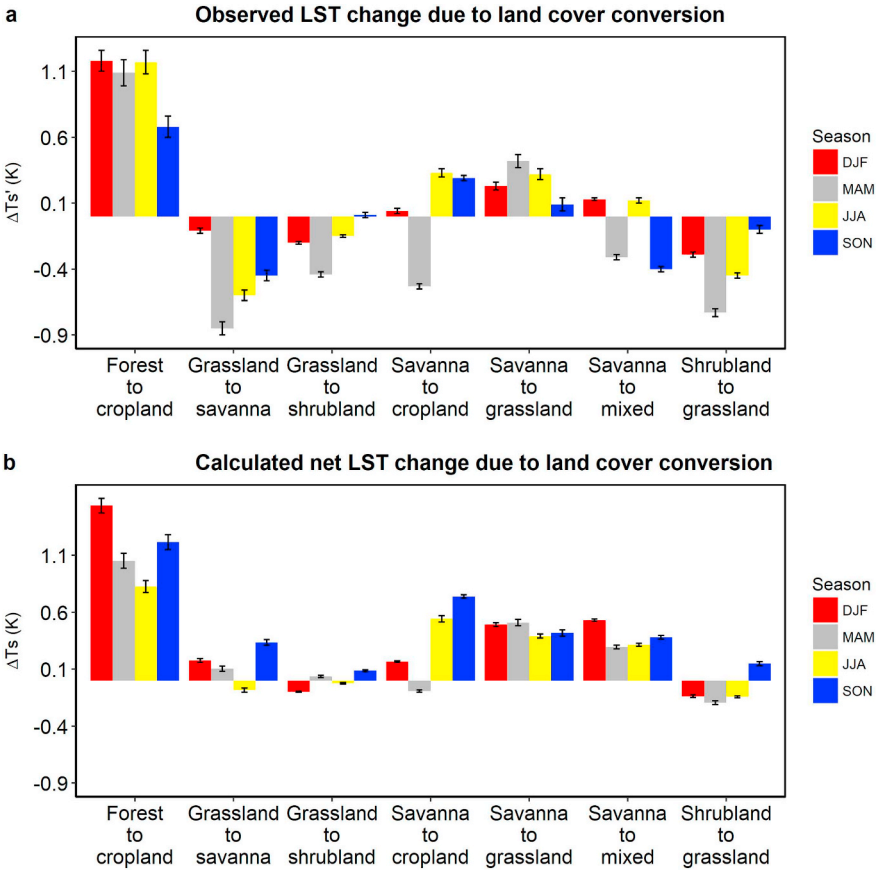

Fig. 8. Mean observed and calculated land surface temperature (LST) change due to land cover conversion in the Horn of Africa between 2001 and 2005 and 2009–2013 across four seasons. In panel (a), LST variability from the background climate signal was removed using LST change from adjacent stable pixels within a distance of 9 km. Panel (b) shows the net LST change from a combined radiative and non-radiative effect. Error bars show 95% confidence interval. DJF = December, January, February; JJA = June, July, August; MAM = March, April, May; SON = September, October, November.

Table 4
Seasonal regional radiative forcing metrics for all land cover change classes in the Horn of Africa during 2001–2013.

Land cover change category	Mean Instantaneous Shortwave Surface Radiative Forcing ($-SW_{in} * \Delta\alpha$) in W m^{-2}				Mean Regional Instantaneous Shortwave Surface Radiative Forcing ($-SW_{in} * \Delta\alpha$) * Ai/At in W m^{-2}			
	DJF	MAM	JJA	SON	DJF	MAM	JJA	SON
Grassland to shrubland	−1.400	−1.000	−0.800	−0.300	−0.027	−0.019	−0.015	−0.006
Savanna to mixed (crop/ vegetation)	−0.800	−0.400	−0.100	−0.020	−0.008	−0.004	−0.001	0.000
Shrubland to grassland	−0.400	−0.200	0.040	0.400	−0.003	−0.002	0.000	0.003
Grassland to savanna	−0.800	−0.900	−0.500	−0.090	−0.004	−0.005	−0.003	0.000
Savanna to grassland	−1.500	−1.200	−0.900	−0.600	−0.006	−0.005	−0.004	−0.003
Savanna to cropland	−1.200	−0.500	0.200	−0.200	−0.004	−0.002	0.001	−0.001
Forest to cropland	−2.600	−1.900	−1.700	−1.700	−0.002	−0.001	−0.001	−0.001
Total	−8.700	−6.100	−3.760	−2.510	−0.056	−0.038	−0.023	−0.008
Annual mean	−5.268				−0.031			

SW_{in} = incoming shortwave radiation; **$\Delta\alpha$** = albedo change; Ai = land surface area covered by land cover change category; At = total land surface area of the study region; DJF = December, January, February; JJA = June, July, August; MAM = March, April, May; SON = September, October, November. Annual mean was calculated from the average of all seasons.

5. Discussion

5.1. Growing season albedo dynamics and their impact on land surface temperature

Albedo increased in taller vegetation (deciduous forest and savanna) but decreased in shorter vegetation (shrubland and grassland) during the growing season. The growing period increase in albedo in taller vegetation can be explained by the increase in canopy near infrared (NIR) reflectance, as green leaves strongly reflect NIR with an intensification in multiple scattering from enhanced canopy development and LAI (Gates, 1965). Canopy development during the growing period affects the amount of NIR and photosynthetically active radiation (PAR) reflectance, which in combination determines the albedo in the growing

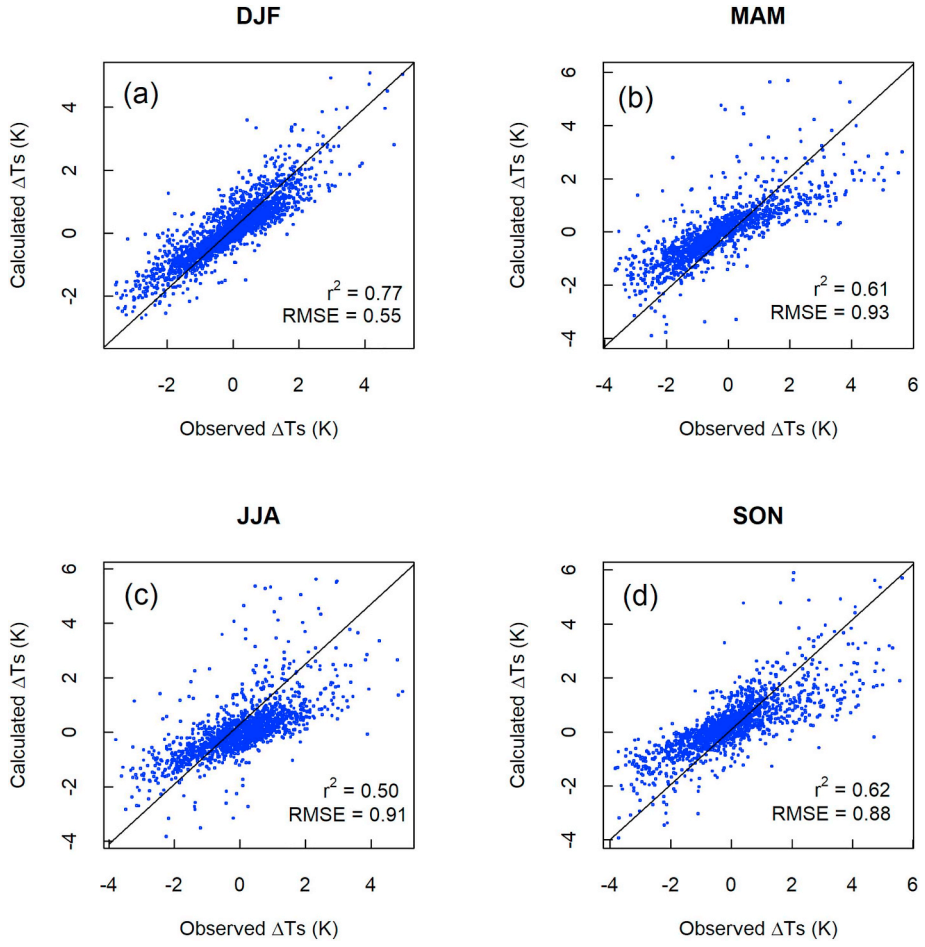

Fig. 9. Comparison of the observed and calculated land surface temperature change due to land cover conversion across four seasons in the Horn of Africa during 2001–2013 based on Moderate Resolution Imaging Spectroradiometer (MODIS) data and the empirical method of Lee et al. (2011). DJF = December, January, February; JJA = June, July, August; MAM = March, April, May; RMSE = root-mean-square error; SON = September, October, November.

season (Richardson et al., 2013). During leaf-out and green-up, PAR reflectance decreases as plants absorb more PAR for photosynthesis, while NIR reflectance increases owing to multiple scattering from the canopy (Ryu et al., 2008; Gates, 1965). In taller vegetation, deciduous forest albedo increased by 8% in the growing period. This result, despite its small magnitude, agrees with previous studies that reported a 20%–50% increase in albedo between the growing season maximum and the non-growing period minimum using ground observation data (Hollinger et al., 2010). Such a variation could be attributed to the different geographic locations, data sources, and local environmental conditions (e.g., background soil color and moisture, understory vegetation albedo, topography). On the other hand, the decrease in albedo during senescence and throughout the non-growing period, in taller vegetation, can be related to the decline in NIR reflectance (Hollinger et al., 2010) and the influence of albedo from the background material (Campbell and Norman, 1998).

In shorter vegetation (shrubland and grassland), the albedo temporal pattern was negatively correlated with LAI. This is likely influenced by the background albedo from soil, which has higher values than that for shorter vegetation (Supplementary Table S1). For instance, during dry and non-growing period, as shrubs drop their leaves and grasses die, a larger soil fraction is exposed to the surface, making the overall albedo higher. During the wet period, on the other hand, vegetation, which has a lower albedo than bare soil, starts to dominate. Furthermore, the increase in soil moisture content in the wet period decreases soil albedo as it is very sensitive to moisture content having the lowest value when the surface is wet (Supplementary Fig. S8; Idso et al., 1975; Wallace et al., 1990). Similar results have been reported for grassland ecosystems where albedo decreases in the growing period and increases quickly after senescence (Ryu et al., 2008; Hollinger et al., 2010). In the shrubland ecosystem, a decrease in albedo from the dry to the wet period was also reported, with a soil wetting being the main cause of the seasonal variation of albedo (Allen et al., 1994). The result, in shorter vegetation, suggests that the albedo of the background material can be important in determining the overall seasonal course of albedo in deciduous ecosystem (Campbell and Norman, 1998; Song, 1999). However, more detailed study using in-situ measurements are needed to understand the extent to which background material albedo affects the overall albedo in the region.

5.2. Seasonality of land surface temperature, albedo, and evapotranspiration

LST seasonality in taller vegetation (e.g., in savanna) had strong negative relations with albedo and ET (Fig. 4). The impact of albedo on LST through reducing available energy was much less compared with that of ET, which considerably diminished the available energy by up to 85% (e.g., Fig. 4a). In shorter vegetation, such as grassland, where LST and albedo seasonal patterns had a positive correlation (Fig. 4b), the warming introduced by an albedo decrease in the wet period was highly outweighed by the ET increase, leading to a reduction in available energy and hence a net surface temperature cooling. These results indicate that, in areas where a strong interaction between LST, albedo and ET is observed, the impacts of albedo on LST seasonality largely vary among vegetation types. In areas where LST did not have significant relations with albedo or ET, temperature is more influenced by the seasonal variation of incoming shortwave radiation, as can be inferred from the significant positive correlation between LST and incoming solar radiation ($r > 0.6$) (Supplementary Fig. S7).

5.3. Impact of land cover changes on albedo, surface radiation balance, and albedo contribution to land surface temperature change

Land cover change showed a consistent increase in mean albedo and a corresponding negative radiative forcing across all seasons, except for shrubland to grassland and savanna to cropland conversions. Despite the average increase in albedo, significant within-class variability was observed, with albedo change ranging from -0.04 to 0.04. The biggest impact on the surface radiative balance and surface temperature through radiative changes is caused by taller vegetation conversions (forest to cropland and savanna to grassland). In these conversion classes, unlike others, around 75% of the total pixels had an increase in albedo, and exhibited the biggest local impact on mean ISRF ($-2.6\ W\ m^{-2}$) and surface temperature cooling by radiative mechanisms of up to -0.12 K.

The overall increase in albedo resulting from the replacement of taller vegetation can be explained by the smaller albedo of taller vegetation compared with brighter shorter vegetation (Betts and Ball, 1997; Hollinger et al., 2010). Despite the average increase, however, up to 25% of the pixels showed decrease in albedo. This likely indicates that albedo is influenced not only by the vegetation structure (LAI and height) but also by the underlying local conditions (such as soil albedo, rainfall, soil color and moisture, etc.) (Bright et al., 2015). In other words, when the background surface is brighter, albedo can increase in taller to shorter vegetation conversions.

The maximum influence of albedo increase on LST occurred in the dry season (DJF) and the smallest in the wet season (SON). This is likely owing to soil moisture content enhancement that increases the amount of incident solar radiation absorbed by the soil system and reduces background surface albedo, leading to a small difference in albedo values compared with the dry period (Idso et al., 1975; Wallace et al., 1990).

The inconsistencies observed in shrubland to grassland conversions can be attributed to the small difference in their albedo values (Supplementary Table S1) together with the influence of background surface albedo, which can be strong in determining the overall albedo in such open-canopy ecosystems (Campbell and Norman, 1998). Furthermore, grassland to savanna conversion, which was expected to show a decrease in albedo compared with savanna to grassland conversion, displayed an opposite result (i.e., an increase in albedo). This can be explained as follows. The conversion classes do not occupy the same geographic location or pixel (i.e. they do not share exactly same background material) and hence the influence of background material can vary depending on the soil color and moisture condition of that location or pixel. This likely can affect and determine the sign and magnitude of albedo change and may lead to an overall average increase in albedo in this conversion class (Campbell and Norman, 1998). Savanna to cropland change can similarly be affected by the background albedo. Moreover, the difficulty in accurately separating small-scale croplands, which often occur mixed with other vegetation at 1 km resolution (Zhang et al., 2005), can cause inconsistencies in the observed results. Further studies using high resolution land cover and soil data are needed to better quantify the actual albedo changes in such conversion areas.

Overall, when the radiative impacts from all land cover changes is considered, the RISRF obtained ($-0.03\ W\ m^{-2}$) was smaller than the global radiative forcing estimate ($-0.09\ W\ m^{-2}$) (Myhre et al., 2005). This is due to three reasons. First, the total area affected by land cover changes in the region during 2001–2013 was around 5%. Second, the biggest local radiative forcing was obtained from forest to cropland and savanna to grassland conversions, which constitute only 1% and 8% of the total land cover change area, respectively. Third, the global estimate represents the period since pre-industrial times (i.e., radiative forcing reported using 1750 as the reference time (Myhre et al., 2013)), and hence compared with this time, the change in land cover over 13-years (2001–2013) can be small.

5.4. Impact of land cover changes on observed land surface temperature changes

Although land cover changes dominantly increased albedo in the region, the net LST displayed mainly warming in taller vegetation

conversions. This opposing result indicates that the radiative cooling effects of land cover change are less influential (maximum −0.12 K in forest to cropland conversions) and are largely outweighed by warming impacts from non-radiative processes (e.g., ET and surface roughness) by a maximum of > 10 times (1.66 K) (Fig. 7a, b). As a result, an overall warming of up to 1.2 K occurred in the region from forest to cropland changes. This result supports earlier findings of observational (Li et al., 2016), and modeling studies (Dickinson and Kennedy, 1992; Zhang and Henderson-Sellers, 1996; Hahmann and Dickinson, 1997) in the tropics, which all reported warming after deforestation.

The warming in forest to cropland conversion in the region is related to a decrease in ET efficiency following leaf area decline and a shift to a shallow rooting system (Davin and de Noblet-Ducoudre, 2010; Bonan, 2008; Claussen et al., 2001). The larger warming during dry period, in comparison with the rainy seasons, can be explained by the enhanced soil moisture and ET, a reduction in the radiation loading due to clouds, and the strong rainfall–vegetation interaction in wet periods (Abera et al., 2018). Moreover, the forests tend to maintain their higher ET efficiency during the dry period through their deep rooting system unlike croplands, and this further increases the difference in warming during dry period (Li et al., 2015).

Savanna to grassland conversions also showed warming across all seasons in the region. The warming in this conversion can be explained by the decline in the woody cover, which can affect the structural and functional properties of the savanna (Hoffmann and Jackson, 2000). Moreover, the consistent warming by non-radiative mechanisms in the region further suggests a decline in ET and surface roughness due to the decrease in woody cover (Fig. 7a). Savannas, compared with grasslands, have higher surface roughness (Miranda et al., 1997), rooting depths (Jackson et al., 1997), as well as LAI, and hence their conversion to grassland leads to warming. Although the impact of savanna to grassland conversion on LST using observational data is rare in the region, modeling studies showed a 0.5 °C mean increase in air temperature in the tropics (Hoffmann and Jackson, 2000). Although LST (radiometric temperature) and air temperature (kinetic temperature) are different in their meaning and magnitude (Jin and Dickinson, 2010), the impact of land cover changes is likely to have similar patterns in these two variables. For instance, several studies have indicated that conversion of woody vegetation (e.g., forest) to grassland/cropland increases both surface and air temperature in the tropics (Alkama and Cescatti (2016), Lee et al. (2011), and Perugini et al. (2017) for an extensive review of the literature). A consistent cooling across seasons was observed when the conversion was the other way around (i.e., grassland to savanna). Such a result further indicates the importance of woody-cover change in determining temperature shift.

In all the rest of the land cover conversion types (i.e., grassland to shrubland or shrubland to grassland, and savanna to mixed (cropland/vegetation) or savanna to cropland), LST had no distinct pattern in the region. In shorter vegetation conversion (grassland to shrubland or vice versa), the lack of clear and consistent warming or cooling across seasons could be due to small differences in surface biophysical properties (e.g., surface roughness, LAI, and ET) between the vegetation types, whereas the inconsistencies in savanna to mixed (cropland/vegetation), which showed an increase in LST during the dry season (DJF) and a decrease in the wet season (MAM), can be attributed to the strong rainfall–vegetation interaction during the wet period, which can cause further cooling by improving the soil moisture and vegetation greening in the region (Abera et al., 2018).

When the impacts of the different land cover change classes on observed LST compared, forest to cropland and savanna to grassland conversions generated more warming than others. Furthermore, the conversion of natural vegetation to cropland (i.e., forest to cropland, savanna to cropland, and savanna to cropland/vegetation) alone constitute 28.8% of the land cover changes in the region. This can cause a considerable anthropogenic impact on the climate through generating a radiative forcing of $-1.5\ W\ m^{-2}$ and a warming of up to 0.45 °C on the average, during the dry season (DJF) in the region (Table 4; Fig. 8). Hence, owing to their stronger impact on climate, future anthropogenic pressure on forests and savannas through cropland land expansion will cause further warming in the region. Besides, when such anthropogenic pressure is coupled with the increasing trends of drought intensity in the region (Nicholson, 2017), climate change impacts can be amplified through additional warming from land cover changes.

Finally, it should be noted that our assessments carry uncertainties associated with the inherent limitations of the data sources used. For example, in land cover change analysis, although we have attempted to minimize the impact of land cover classification accuracy (~75%) on the results by focusing on changes between stable pixels in the first and last five years of 2001–2013, incorrectly identified pixels can exist in the analysis and this might introduce uncertainty in the results. However, the impact of such uncertainty has been minimized by taking the average value in each land cover conversion class. Also, the use of the empirical method of Lee et al. (2011) to calculate LST change from individual contribution by radiative and non-radiative processes using satellite observation data can be affected by the inherent limitations of the data (i.e., LST changes within $1\ km^2$ pixels were assumed homogeneous due to a limitation of the spatial resolution, but in reality LST change can vary as long as land cover type differs within the $1\ km^2$ pixels). Furthermore, in quantifying the uncertainty in our LST estimation, despite the unavailability of in-situ flux data in the region, we tested and showed the robustness of the method by comparing the calculated LST change from the model with the observed LST change from the MODIS LST. The results showed reasonably good agreement ($r^2 = 0.77$), particularly during the dry period (DJF). Nonetheless, the future availability of ground flux tower data across different land cover types in the region will help improve quantification of the uncertainty in such a method.

6. Conclusion

In this study, we investigated how radiative mechanisms associated with seasonal dynamics in natural vegetation and abrupt land cover changes caused by anthropogenic activities may affect LST changes. In taller vegetation (forest and savanna), albedo increased during the growing period, causing a decline in net shortwave radiation of $-10\ W\ m^{-2}$; whereas in shorter vegetation (grassland and shrubland), albedo decreased, resulting in an increase in net shortwave radiation of $7\ W\ m^{-2}$. The albedo cooling and warming impact during the growing period in taller and shorter vegetation, respectively, were however highly outweighed by ET cooling, which had a dominating influence on LST seasonality in the region.

Land cover changes caused an average increase in albedo, with a maximum surge observed in the dry period (DJF). The albedo changes from all land cover changes together generated a regional instantaneous shortwave surface radiative forcings of $-0.03\ W\ m^{-2}$. Regardless of the small regional forcing, the mean instantaneous local surface radiative forcings in forest to cropland ($-2.6\ W\ m^{-2}$) and savanna to grassland ($-1.5\ W\ m^{-2}$) conversions and their contributions to LST cooling (−0.12 K and −0.09 K) were bigger than other conversion classes, respectively. Despite such LST cooling, however, these conversion classes displayed the largest average observed LST warming of up to 1.2 K and 0.4 K, respectively. These warming impacts are due to the dominant influence of non-radiative mechanisms through a reduction in ET and surface roughness following woody cover decline, which largely offset the albedo cooling effect. The increase or decrease in woody cover was shown to largely determine the observed LST change in the region as indicated in the savanna to grassland and grassland to savanna conversions that displayed consistent average warming and cooling across seasons, respectively.

Overall, the results showed that the radiative impact of albedo change on LST seasonality, either in the growing period or during land cover transitions, was relatively small in comparison with the influence

of non-radiative processes (e.g., ET). Hence, our results highlight the importance of accounting for non-radiative mechanisms for a better quantification and understanding of the impacts of land cover change on climate, as well as for setting effective land use policies and mitigation strategies in the region.

Acknowledgements

The first author, Mr. Temesgen A. Abera, acknowledges funding from the Ethiopian government under project number INSA9/AT34/1630/16. Professor Petri Pellikka would like to acknowledge funding from the Academy of Finland for the project 'Environmental sensing of ecosystem services for developing climate smart landscape framework to improve food security in East Africa' (decision number 318645). Miina Rautiainen acknowledges funding from the Academy of Finland (decision number 286390). Eduardo Maeda acknowledges funding from the Academy of Finland (decision numbers 318252 and 319905). Furthermore, we thank three anonymous reviewers for their useful comments on the manuscript.

Appendix A. Supplementary data

Supplementary data to this article can be found online at https://doi.org/10.1016/j.rse.2018.11.024.

References

Abera, T.A., Heiskanen, J., Pellikka, P.K., Maeda, E.E., 2018. Rainfall-vegetation interaction regulates temperature anomalies during extreme dry events in the horn of Africa. Glob. Planet. Chang. 167, 35–45. https://doi.org/10.1016/j.gloplacha.2018.05.002.

Alkama, R., Cescatti, A., 2016. Biophysical climate impacts of recent changes in global forest cover. Science 351 (6273), 600–604. https://doi.org/10.1126/science.aac8083.

Allen, S.J., Wallace, J.S., Gash, J.H.C., Sivakumar, M.V.K., 1994. Measurements of albedo variation over natural vegetation in the Sahel. Int. J. Climatol. 14 (6), 625–636. https://doi.org/10.1002/joc.3370140603.

Bastiaanssen, W.G.M., 2000. SEBAL-based sensible and latent heat fluxes in the irrigated Gediz Basin, Turkey. J. Hydrol. 229 (1), 87–100. https://doi.org/10.1016/S0022-1694(99)00202-4.

Betts, A.K., Ball, J.H., 1997. Albedo over the boreal forest. J. Geophys. Res.-Atmos. 102 (D24), 28901–28909. https://doi-org.libproxy.helsinki.fi/10.1029/96JD03876.

Bonan, G.B., 2008. Forests and climate change: forcings, feedbacks, and the climate benefits of forests. Science 320 (5882), 1444–1449. https://doi.org/10.1126/science.1155121.

Bright, Ryan M., 2015. Metrics for biogeophysical climate forcings from land use and land cover changes and their inclusion in life cycle assessment: a critical review. Environ. Sci. Technol. 49 (6), 3291–3303. https://doi.org/10.1021/es505465t.

Bright, Ryan M., Zhao, Kaiguang, Jackson, Robert B., Cherubini, Francesco, 2015. Quantifying surface albedo and other direct biogeophysical climate forcings of forestry activities. Glob. Chang. Biol. 3246–3266. https://doi.org/10.1111/gcb.12951.

Bright, R.M., Davin, E.L., O'Halloran, T.L., Pongratz, J., Zhao, K., Cescatti, A., 2017. Local surface temperature response to land cover and management change driven by non-radiative processes. Nat. Clim. Chang. 7 (296). https://doi.org/10.1038/nclimate3250. (Forthcoming).

Brink, A.B., Bodart, C., Brodsky, L., Defourney, P., Ernst, C., Donney, F., ... Tuckova, K., 2014. Anthropogenic pressure in East Africa-monitoring 20 years of land cover changes by means of medium resolution satellite data. Int. J. Appl. Earth Obs. Geoinf. 28 (1), 60–69. https://doi.org/10.1016/j.jag.2013.11.006.

Campbell, G.S., Norman, J.M., 1998. An Introduction to Environmental Biophysics. Springer, New York (286 pp).

Claussen, M., Brovkin, V., Ganopolski, A., 2001. Biogeophysical versus biogeochemical feedbacks of large-scale land cover change. Geophys. Res. Lett. 28 (6), 1011–1014. https://doi.org/10.1029/2000GL012471.

Cleugh, H.A., Leuning, R., Mu, Q., Running, S.W., 2007. Regional evaporation estimates from flux tower and MODIS satellite data. Remote Sens. Environ. 106 (3), 285–304. https://doi.org/10.1016/j.rse.2006.07.007.

Davin, E.L., de Noblet-Ducoudre, N., 2010. Climatic impact of global-scale deforestation: radiative versus nonradiative processes. J. Clim. 23 (1), 97–112. https://doi.org/10.1175/2009JCLI3102.1.

Dickinson, R.E., Kennedy, P., 1992. Impacts on regional climate of Amazonian deforestation. Geophys. Res. Lett. 19 (19), 1947–1950. https://doi.org/10.1029/92GL01905.

Friedl, M.A., Sulla-Menashe, D., Tan, B., Schneider, A., Ramankutty, N., Sibley, A., Huang, X., 2010. MODIS collection 5 global land cover: algorithm refinements and characterization of new datasets. Remote Sens. Environ. 114 (1), 168–182. https://doi.org/10.1016/j.rse.2009.08.016.

Gates, D.M., 1965. Energy, plants, and ecology. Ecology 46 (1–2), 1–13. https://doi.org/10.2307/1935252.

GMAO (Global Modeling and Assimilation Office), 2015. MERRA-2 tavgM_2d_slv_Nx: 2d, Monthly Mean, Time-averaged, Single-level, Assimilation, Single-Level Diagnostics V5.12.4. Goddard Earth Sciences Data and Information Services Center (GES DISC), Grecampenbelt, MD, USA. https://doi.org/10.5067/AP1B0BA5PD2K. (https://disc.gsfc.nasa.gov/datasets/M2TMNXSLV_V5.12.4/summary, accessed November 08, 2017).

Goddard Earth Sciences Data and Information Services Center (GES DISC), 2016. TRMM (TMPA) Precipitation 1 month 0.25 degree × 0.25 degree V7. http://disc.gsfc.nasa.gov/datacollection/TRMM_3B43_V7.shtml, Accessed date: 21 April 2018.

Hahmann, A.N., Dickinson, R.E., 1997. RCCM2-BATS model over tropical South America: applications to tropical deforestation. J. Clim. 10, 1944–1964. https://doi.org/10.1175/1520-0442(1997)010<1944:RBMOTS>2.0.CO;2.

Henderson-Sellers, A., Wilson, M.F., 1983. Albedo observations of the earth's surface for climate research. Philos. Trans. R. Soc. Lond. A, Math. Phys. Sci. 309 (1508), 285–294. http://www.jstor.org/stable/37357.

Hoffmann, W.A., Jackson, R.B., 2000. Vegetation–climate feedbacks in the conversion of tropical savanna to grassland. Am. Meteorol. Soc. 13 (9), 1593–1602. https://doi.org/10.1175/1520-0442(2000)013<1593:VCFITC>2.0.CO;2.

Hollinger, D.Y., Ollinger, S.V., Richardson, A.D., Meyers, T.P., Dail, D.B., Martin, M.E., ... Verma, S.V., 2010. Albedo estimates for land surface models and support for a new paradigm based on foliage nitrogen concentration. Glob. Chang. Biol. 16, 696–710. https://doi.org/10.1111/j.1365-2486.2009.02028.x.

Idso, S.B., Jackson, R.D., Reginato, R.J., Kimball, B.A., Nakayama, F.S., 1975. The dependence of bare soil albedo on soil water content. J. Appl. Meteorol. 14 (1), 109–113. https://doi.org/10.1175/1520-0450(1975)014<0109:TDOBSA>2.0.CO;2.

Indeje, M., Semazzi, F.H.M., Ogallo, L.J., 2000. ENSO signals in East African rainfall seasons. Int. J. Climatol. 20 (1), 19–46. https://doi.org/10.1002/(SICI)1097-0088(200001)20:1<19::AID-JOC449>3.0.CO;2-0.

Jackson, R.B., Mooney, H.A., Schulze, E.D., 1997. A global budget for fine root biomass, surface area, and nutrient contents. Proc. Natl. Acad. Sci. 94 (14), 7362–7366. https://doi.org/10.1073/pnas.94.14.7362.

Jin, M., Dickinson, R.E., 2010. Land surface skin temperature climatology: benefitting from the strengths of satellite observations. Environ. Res. Lett. 5 (4), 44004. https://doi.org/10.1088/1748-9326/5/4/044004.

Lee, X., Goulden, M.L., Hollinger, D.Y., Barr, A., Black, T.A., Bohrer, G., ... Zhao, L., 2011. Observed increase in local cooling effect of deforestation at higher latitudes. Nature 479 (7373), 384–387. https://doi.org/10.1038/nature10588.

Li, Y., Zhao, M., Motesharrei, S., Mu, Q., Kalnay, E., Li, S., 2015. Local cooling and warming effects of forests based on satellite observations. Nat. Commun. 6, 6603. https://doi.org/10.1038/ncomms7603.

Li, Y., Zhao, M., Mildrexler, D.J., Motesharrei, S., Mu, Q., Kalnay, E., ... Wang, K., 2016. Potential and actual impacts of deforestation and afforestation on land surface temperature. J. Geophys. Res.-Atmos. https://doi.org/10.1002/2016JD024969.

Liang, S., Liu, Q., 2012. Global Land Surface Products. Albedo Product Data Collection (1985–2010). Beijing Normal Universityhttps://doi.org/10.6050/glass863.3001.db.

Liu, J., Schaaf, C., Strahler, A., Jiao, Z., Shuai, Y., Zhang, Q., ... Dutton, E.G., 2009. Validation of moderate resolution imaging spectaroradiometer (MODIS) albedo retrieval algorithm: dependence of albedo on solar zenith angle. J. Geophys. Res. 114, 1–11. https://doi.org/10.1029/2008JD009969.

Luyssaert, S., et al., 2014. Land management and land-cover change have impacts of similar magnitude on surface temperature. Nat. Clim. Chang. 4, 389–393. https://doi.org/10.1038/NCLIMATE2196.

Michael, G.B., Santha, A., Lawrence, C., Richard, C., Clara, D., Ronald, G., ... Suarez, Max, 2015. MERRA-2: initial evaluation of the climate. Technical report series on global modeling and data assimilation. Vol. 43. https://gmao.gsfc.nasa.gov/pubs/docs/Vernieres589.pdf, Accessed date: 2 May 2018.

Miranda, A.C., Miranda, H.S., Lloyd, J., Grace, J., Francey, R.J., Mcintyre, J.A., ... Brass, J.B., 1997. Fluxes of carbon, water, and energy over Brazilian cerrado: an analysis using eddy covariance and stable isotopes. Plant Cell Environ. 20 (3), 315–328. https://doi.org/10.1046/j.1365-3040.1997.d01-80.x.

Moore, K.E., Fitzjarrald, D.R., Sakai, R.K., 1996. Seasonal variation in radiative and turbulent exchange at a deciduous forest in Central Massachusetts. J. Appl. Meteorol. 35 (1), 122–134. https://doi.org/10.1175/1520-0450(1996)035<0122.

Myhre, G., Kvaleva, M.M., Schaaf, C.B., 2005. Radiative forcing due to anthropogenic vegetation change based on MODIS surface albedo data. Geophys. Res. Lett. 32, 2–5. https://doi.org/10.1029/2005GL024004.

Myhre, G., Shindell, D., Bréon, F.-M., Collins, W., Fuglestvedt, J., Huang, J., Zhang, D. Koch… H., 2013. Anthropogenic and natural radiative forcing. In: Stocker, T.F., Qin, D., Plattner, G.-K., Tignor, M., Allen, S.K., Boschung, J., Nauels, A., Xia, Y., Bex, V., Midgley, P.M. (Eds.), Climate Change 2013: The Physical Science Basis. Contribution of Working Group I to the Fifth Assessment Report of the Intergovernmental Panel on Climate Change. Cambridge University Press, Cambridge, United Kingdom and New York, NY, USA.

Myneni, R., Knyazikhin, Y., Park, T., 2015. MCD15A2H MODIS/Terra + Aqua Leaf Area Index/FPAR 8-day L4 Global 500m SIN Grid V006. NASA EOSDIS Land Processes DAAChttps://doi.org/10.5067/MODIS/MCD15A2H.006.

NASA LP DAAC, 2014. MCD43B1 BRDF-Albedo Model Parameters 8-Day L3 Global 1 km. Version 5. NASA EOSDIS Land Processes DAAC, USGS Earth Resources Observation and Science (EROS) Center, Sioux Falls, South Dakota. https://lpdaac.usgs.gov, Accessed date: 10 December 2016.

NASA LP DAAC, 2016a. MCD12Q1 Land Cover Type Yearly L3 Global 500 m SIN Grid. Version 051. NASA EOSDIS Land Processes DAAC. USGS Earth Resources Observation and Science (EROS) Center, Sioux Falls, South Dakota. https://lpdaac.

usgs.gov, Accessed date: 15 October 2017.
NASA LP DAAC, 2016b. MCD43B3 Black-sky and white-sky albedo 8-Day L3 Global 1 km SIN Grid. Version 6. NASA EOSDIS Land Processes DAAC, USGS Earth Resources Observation and Science (EROS), Center, Sioux Falls, South Dakota. https://lpdaac.usgs.gov, Accessed date: 15 October 2017.
Nicholson, S.E., 1996. A Review of Climate Dynamics and Climate Variability in Eastern Africa. American Geosciences Institute.
Nicholson, S.E., 2017. Climate and climatic variability of rainfall over eastern Africa. Rev. Geophys. 55, 590–635. https://doi.org/10.1002/2016RG000544.
Ogallo, L.J., 1988. Relationships between seasonal rainfall in East Africa and the southern oscillation. J. Climatol. 8 (1), 31–43. https://doi.org/10.1002/joc.3370080104.
Pellikka, P.K.E., Heikinheimo, V., Hietanen, J., Schäfer, E., Siljander, M., Heiskanen, J., 2018. Impact of land cover change on aboveground carbon stocks in Afromontane landscape in Kenya. Appl. Geogr. 94, 178–189. https://doi.org/10.1016/j.apgeog.2018.03.017.
Peng, S.-S., Piao, S., Zeng, Z., Ciais, P., Zhou, L., Li, L.Z.X., Zeng, H., 2014. Afforestation in China cools local land surface temperature. Proc. Natl. Acad. Sci. 111 (8), 2915–2919. https://doi.org/10.1073/pnas.1315126111.
Perugini, L., Caporaso, L., Marconi, S., Cescatti, A., Quesada, B., De Noblet-Ducoudré, N., House, J.I., Arneth, A., 2017. Biophysical effects on temperature and precipitation due to land cover change. Environ. Res. Lett. 12 (5). https://doi.org/10.1088/1748-9326/aa6b3f.
Pfeifroth, Uwe, Kothe, Steffen, Müller, Richard, Trentmann, Jörg, Hollmann, Rainer, Fuchs, Petra, Werscheck, Martin, 2017. Surface radiation data set - Heliosat (SARAH) - edition 2. In: Satellite Application Facility on Climate Monitoring, https://doi.org/10.5676/EUM_SAF_CM/SARAH/V002.
Pielke Sr., R.A., Avissar, R., Raupach, M., Dolman, A.J., Zeng, X., Denning, A.S., 1998. Interactions between the atmosphere and terrestrial ecosystems: influence on weather and climate. Glob. Chang. Biol. 4 (5), 461–475. https://doi.org/10.1046/j.1365-2486.1998.t01-1-00176.x.
Richardson, A.D., Keenan, T.F., Migliavacca, M., Ryu, Y., Sonnentag, O., Toomey, M., 2013. Climate change, phenology, and phenological control of vegetation feedbacks to the climate system. Agric. For. Meteorol. 169, 156–173. https://doi.org/10.1016/j.agrformet.2012.09.012.
Jin, Y., Roy, D.P., 2005. Fire-induced albedo change and its radiative forcing at the surface in northern Australia. Geophys. Res. Lett. 32 (13). https://doi.org/10.1029/2005GL022822.
Running, S., Mu, Q., Zhao, M., 2017. MOD16A2 MODIS/Terra Net Evapotranspiration 8-Day L4 Global 500m SIN Grid V006. NASA EOSDIS Land Processes DAAChttps://doi.org/10.5067/MODIS/MOD16A2.006.
Ryu, Y., Baldocchi, D.D., Ma, S., Hehn, T., 2008. Interannual variability of evapotranspiration and energy exchange over an annual grassland in California. J. Geophys. Res.-Atmos. 113 (D9). https://doi.org/10.1029/2007JD009263.
Schaaf, C.B., Gao, F., Strahler, A.H., Lucht, W., Li, X., Tsang, T., ... Roy, D., 2002. First operational BRDF albedo nadir reflectance products from MODIS. Remote Sens. Environ. 83 (1–2), 135–148. https://doi.org/10.1016/S0034-4257(02)00091-3.
Schwartz, M.D., 1992. Phenology and springtime surface-layer change. Mon. Weather Rev. 120, 2570–2578. https://doi.org/10.1175/1520-0493(1992)120<2570:PASSLC>2.0.CO;2.
Song, J., 1999. Phenological influences on the albedo of prairie grassland and crop fields. Int. J. Biometeorol. 42 (3), 153–157. https://doi.org/10.1007/s004840050099.
Wallace, J.S., Gash, J.H.C., Sivakumar, M.V.K., 1990. Preliminary measurements of net radiation and evaporation over bare soil and fallow bushland in the Sahel. Int. J. Climatol. 10 (2), 203–210. https://doi.org/10.1002/joc.3370100207.
Wan, Z., Zhang, Y., Zhang, Q., Li, Z., 2002. Validation of the land surface temperature products retrieved from Terra Moderate Resolution Imaging Spectroradiometer data. Remote Sens. Environ. 83 (1), 163–180. https://doi.org/10.1016/S0034-4257(02)00093-7.
Wan, Z., Hook, S., Hulley, G., 2015. MOD11A2 MODIS/Terra Land Surface Temperature/Emissivity 8-Day L3 Global 1km SIN Grid V006. NASA EOSDIS LP DAAChttps://doi.org/10.5067/modis/mod11a2.006.
White, F., 1983. The vegetation of Africa: a descriptive memoir to accompany the UNESCO/AETFAT/UNSO vegetation map of Africa. Nat. Resour. Res. 20. https://doi.org/10.2307/2260340.
Williamson, Scott N., Barrio, Isabel C., Hik, David S., Gamon, John A., 2016. Phenology and species determine growing-season albedo increase at the altitudinal limit of shrub growth. Glob. Chang. Biol. 3621–3631. https://doi.org/10.1111/gcb.13297.
Yang, W., Tan, B., Huang, D., Rautiainen, M., Shabanov, N.V., Wang, Y., ... Myneni, R.B., 2006. MODIS leaf area index products: from validation to algorithm improvement. IEEE Trans. Geosci. Remote Sens. 44 (7), 1885–1898. https://doi.org/10.1109/TGRS.2006.871215.
Zhang, H., Henderson-Sellers, A., 1996. Impacts of tropical deforestation. Part I: process analysis of local climatic change. J. Clim. 9 (7), 1497–1517. https://doi.org/10.1175/1520-0442(1996)009<1497:IOTDPI>2.0.CO;2.
Zhang, X., Friedl, M.A., Schaaf, C.B., Strahler, A.H., Liu, Z., 2005. Monitoring the response of vegetation phenology to precipitation in Africa by coupling MODIS and TRMM instruments. J. Geophys. Res. D: Atmos. 110 (12), 1–14. https://doi.org/10.1029/2004JD005263.